List-Mode Reconstruction with System Modeling Derived from Projections

Andrew J. Reader, Florent C. Sureau, Claude Comtat, Irène Buvat and Régine Trébossen

***Abstract*– Image reconstruction direct from list-mode data can preserve and utilize all the precision and accuracy of the substantial volume of data acquired by high resolution dynamic emission tomography systems. However, there remains a need for a full system modeling methodology to account for randoms, scatter, attenuation and normalization within list-mode reconstruction. Modeling and/or correcting for these effects has been substantially researched and developed for sinogram-based reconstructions, and so this work considers an Expectation Maximisation (EM) reconstruction algorithm which uses the list-mode data directly, but also accesses projection data to determine the randoms, scatter, attenuation and normalization components of the system model. Using the example of the High Resolution Research Tomograph (HRRT, CTI PET Systems) scanner and the sinogram corrections available with this system, it is found that it is necessary to spatially align each list-mode event with the nearest sinogram bin in order to avoid a sampling mismatch when using the sinogram-data based corrections. Simulation results indicate that provided projections with high enough sampling are used, this compromise of the spatial precision of the list-mode data is not of significance for the HRRT, and moreover is a much less important effect compared to the inclusion or exclusion of an image space resolution model. The storage and temporal sampling advantages of the list-mode data are however retained.**

I. Introduction

THE continuing advancements in high resolution emission tomography instrumentation have resulted in systems which are able to acquire substantial quantities of time-dependent data with high spatio-temporal precision and accuracy. However, conventional reconstruction and processing methodologies often require the acquired data to be in histogram / projection format – which for high resolution systems often involves an undesirable reduction in both temporal and spatial sampling, in order to obtain computationally practical data set sizes. To avoid this issue, direct list-mode data reconstruction algorithms have been devised (e.g. [1]-[4]). Unlike the more established projection-data based reconstruction algorithms however, the list-mode techniques are still in need of a full system modeling and data correction methodology. This work considers a hybrid approach, combining a list-mode reconstruction with data modeling / correction data derived from 3D sinogram data sets. In order to directly use the normalization, attenuation, randoms and scatter sinograms (without modification), it is necessary to spatially align (i.e. spatially "bin") each list-mode event during reconstruction, to avoid artifacts arising from a sampling mismatch between the list-mode and projection data. The significance of this loss in spatial precision is assessed and compared with another key factor which is crucial to reconstructed image quality: inclusion or exclusion of a spatial resolution model.

Manuscript received November 11, 2005.

A.J. Reader is with the School of Chemical Engineering and Analytical Science (SCEAS) at the University of Manchester, Manchester, PO BOX 88, M60 1QD, United Kingdom (e-mail: A.J.Reader@manchester.ac.uk).

F. C. Sureau, C. Comtat and R. Trébossen are with the Service Hospitalier Frédéric Joliot, CEA/DSV/DRM, Orsay, France

F. C. Sureau is also with Siemens Medical Solutions Saint-Denis, France.

I. Buvat is with UMR 678 INSERM - UPMC, CHU Pitié-Salpêtrière, Paris, France

II. Theory

A. The Forward Model and EM Algorithms

The particular case of static reconstruction of 3D positron emission tomography (PET) data will be considered. The forward model giving the expectation **q** for the I-dimensional (I-D) acquired data vector **p** can be written as

$$\mathbf{q} = \mathbf{ANXHf} + \mathbf{s} + \mathbf{r} \qquad (1)$$

where **f** is a J-D vector holding the amplitudes of J spatial-basis functions (used to represent the spatial radioactivity distribution), **H** is a $J \times J$ matrix used to model positron range (and possibly other resolution degrading effects), **X** is the discrete $I \times J$ x-ray transform which integrates along lines through the object, **A** and **N** are $I \times I$ diagonal matrices modeling the attenuation and normalization effects and **s** and **r** are I-D vectors holding the scatter and randoms contribution to the expected data. The matrix **H** can also be used in an *approximate* way to model other resolution degrading effects (such as photon acollinearity and detector resolution). Each element p_i in the measured data vector **p** indicates the number of times an event was detected in each unique system line of response (LOR) i. For high resolution systems the data vector **p** (which retains all spatial sampling accuracy) will be very sparse and so list-mode data is often used, which only records the LORs present in a particular scan / acquisition of data. The use of **p** to represent the list-mode data is still valid, so long as the accuracy and precision is fully retained in the sparse vector **p**.

To use the well-established projection-data based algorithms for reconstruction of an estimate of **f** from **p**, the data need to be binned into projections, normally involving temporal and spatial sampling losses. The binning operation will be represented by an $R \times I$ matrix **B** which operates on an I-D data vector of LORs to give a reduced R-D vector of bins (there are usually many LORs which contribute to a single projection bin). In this case the forward model becomes

$$\mathbf{Bq} = \mathbf{BANXHf} + \mathbf{Bs} + \mathbf{Br} \qquad (2)$$

The EM reconstruction algorithm, which does not preprocess the measured data (hence preserving the Poisson statistics), is given by

$$\mathbf{f}^{k+1} = \mathbf{f}^{k} \frac{\mathbf{H}^T\mathbf{X}^T\mathbf{N}\mathbf{A}\mathbf{B}^T\left\{\dfrac{\mathbf{Bp}}{\mathbf{BANXHf}^k + \mathbf{Bs} + \mathbf{Br}}\right\}}{\mathbf{H}^T\mathbf{X}^T\mathbf{N}\mathbf{A}\mathbf{B}^T\mathbf{1}} \qquad (3)$$

where in this notation the product and division of vectors are each understood to be carried out in an element-by-element fashion, **1** is an *I*-D vector containing elements all equal to 1 and note that $\mathbf{N}^T$=**N** and $\mathbf{A}^T$=**A** has been used. Quite often the attenuation and normalization diagonal $I\times I$ matrices **A** and **N** are only available in the binned *R*-D space (whereby **A** and **N** are replaced by the $R\times R$ matrices $\mathbf{A}_B$ and $\mathbf{N}_B$), so as an approximation the following algorithm

$$\mathbf{f}^{k+1} = \mathbf{f}^{k} \frac{\mathbf{H}^T\mathbf{X}_B^T\mathbf{N}_B\mathbf{A}_B\left\{\dfrac{\mathbf{Bp}}{\mathbf{A}_B\mathbf{N}_B\mathbf{X}_B\mathbf{Hf}^k + \mathbf{Bs} + \mathbf{Br}}\right\}}{\mathbf{H}^T\mathbf{X}_B^T\mathbf{N}_B\mathbf{A}_B\mathbf{1}} \qquad (4)$$

is used, where each projection bin is treated as if it contained a single LOR located exactly in the centre of the bin, and the $R\times J$ matrix $\mathbf{X}_B$ performs line integrals only along the reduced set of *R* lines corresponding to each projection bin centre (rather than all the *I* lines corresponding to each actual system LOR). The data sets **Bs** and **Br** are normally estimated directly (i.e. **s** and **r**, with their prohibitively high sampling, are not normally calculated, just as **A** and **N** are not normally found). An intuitive modification of equation (4) to operate on list-mode data can be obtained by using the correction vectors and matrices (**Bs**, **Br** and $\mathbf{A}_B$ and $\mathbf{N}_B$) without modification, yet retaining the sampling accuracy of each event LOR in the list-mode data – i.e. using the matrix product **BX** rather than $\mathbf{X}_B$:

$$\mathbf{f}^{k+1} = \mathbf{f}^{k} \frac{\mathbf{H}^T\mathbf{X}^T\mathbf{B}^T\mathbf{N}_B\mathbf{A}_B\left\{\dfrac{\mathbf{Bp}}{\mathbf{A}_B\mathbf{N}_B\mathbf{BXHf}^k + \mathbf{Bs} + \mathbf{Br}}\right\}}{\mathbf{H}^T\mathbf{X}^T\mathbf{B}^T\mathbf{N}_B\mathbf{A}_B\mathbf{1}} \qquad (5)$$

Equation (5) is very impractical however, requiring the use of $\mathbf{B}^T$ – which operates on each of the *R* sinogram bins to produce every single one of the *I* system LORs corresponding to that bin (a computationally demanding approach). In this work a simpler, computationally practical, algorithm is chosen which is virtually identical to equation (4) except for the fact that the data vector p is accessed event by event. Each event is spatially aligned with its nearest corresponding projection bin – hence compromising the spatial sampling of the data (the significance of which is assessed in this work), but therefore allowing use of the correction vectors and matrices (**Bs**, **Br** and $\mathbf{A}_B$ and $\mathbf{N}_B$) without modification. If the list-mode data are divided into λ subsets of equal size ($\mathbf{p}_1$, $\mathbf{p}_2$, … $\mathbf{p}_\lambda$), each subset being used to perform an image update, the following algorithm is obtained:

$$\mathbf{f}^{k+1} = \mathbf{f}^{k} \frac{\mathbf{H}^T\mathbf{X}_B^T\mathbf{N}_B\mathbf{A}_B\left\{\lambda\dfrac{\mathbf{Bp}_\lambda}{\mathbf{A}_B\mathbf{N}_B\mathbf{X}_B\mathbf{Hf}^k + \mathbf{Bs} + \mathbf{Br}}\right\}}{\mathbf{H}^T\mathbf{X}_B^T\mathbf{N}_B\mathbf{A}_B\mathbf{1}} \qquad (6)$$

where the scale factor λ is required to compensate for the reduced number of events used in each iterative update (the vectors **Bs** and **Br** assume that all the data are used in each update).

III. Methods

A. Simulation Phantom

A simple Monte Carlo simulation for the High Resolution Research Tomograph (HRRT) [5] was coded to generate list-mode data, incorporating the scanner geometry (with detector gaps), but excluding effects such as attenuation, scatter and randoms. The primary goals were to investigate the relative importance between raw data accuracy (i.e. the choice between projection data spatial sampling accuracy and that of pure list-mode data, which contains no sampling compromises) and system modeling (in this study, the inclusion or exclusion of spatial resolution modeling). The simulation phantom used for this assessment consisted of a cylinder of diameter 234.5 mm and length 150.5 mm, with a hot rim (5.7 mm thickness). The cylinder contained 2 line sources, one parallel to the central z-axis, but displaced radially by 65 mm, and one located in a transverse slice, displaced axially by 50 mm. Both line sources were 117 mm long, and 1 mm in diameter. In addition, a 7×7 cluster of 1 mm diameter point sources, each separated by 5 mm and arranged in a square formation was included within the cylinder, along with 3 spheres of radius 12.5 mm. Fig. 1 shows a selection of sagittal, coronal and transverse sections of the phantom. In order to approximately simulate resolution degrading effects (such as positron range, photon acollinearity, limited detector resolution) a radially displaced annihilation position (i.e. displaced from the site of positron emission) was obtained by taking a sample from a 1D radial Gaussian probability density function of 2 mm FWHM and with a mean equal to the positron emission location. One hundred million events were simulated.

The data were reconstructed into matrices of size 256×256×208, with and without an image space resolution model (i.e. with and without the matrix **H**), using two iterations of 32 subsets of the EM algorithm. In addition, the impact of data accuracy was examined, by using the data either as pure list-mode, or as list-mode corresponding to the sampling level of span 3 or span 9 sinograms. Span refers to the number of copolar angular bins which are summed, which reduces the size of the full set of sinograms. To emulate the reduction in spatial sampling which would be incurred if sinograms were used, each list-mode event was spatially aligned with its nearest corresponding sinogram bin – replacing the exact list-mode coordinates by the coordinates of the centre of the sinogram bin. Hence 6 reconstructions of the simulated data set were carried out: for 2 types of system model (with and without resolution modeling), each with 3 levels of data accuracy (pure list-mode, span 3 and span 9).

The full width at half maximum (FWHM) of the reconstructed line source profiles was used as a resolution measure. The uniform background activity distribution was used as a measure of image noise: the variation of voxel intensity as a function of position was summarized using a

simple spatial standard deviation calculation, divided by the mean of the activity within this uniform volume.

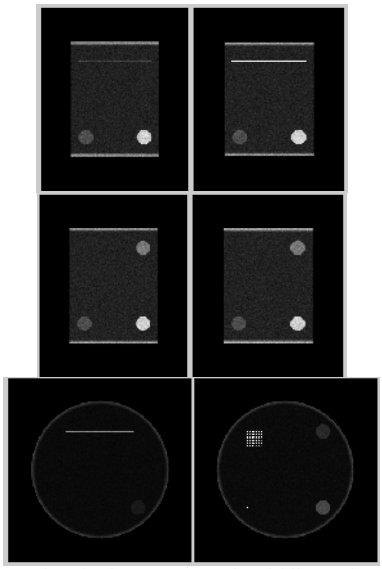

Fig. 1. A selection of sagittal (top), coronal (middle) and transverse (bottom) slices from the phantom used for the tests. The cylindrical phantom contained 3 spheres, 49 point sources arranged in a square (bottom right sub-figure) and two line sources. In this study only the line and point sources were used to assess resolution, with the uniform background region being used to assess image noise.

B. Measured Data

To determine an approximate image space resolution modeling kernel, data from a point source acquisition were reconstructed using the algorithm without **H**. A resolution kernel was then found through optimization of the parameters α and β of the following exponential function:

$$f(r) = \frac{1}{N}\left(\beta + \exp(-\alpha r)\right) \qquad (7)$$

with N calculated such that the area under the function was equal to one. The optimization process modeled the 3D convolution of the point source with this kernel, and the parameters of the kernel were found such that a least squares fit between the 3D reconstruction and the convolution model was obtained.

In addition a Jaszczak phantom was scanned (cylinder of inner length 187 mm, inner diameter 196 mm, 1.4 mCi ^{18}F). One hundred and fifty million events from the first 5 minutes of data acquisition were used to obtain a reconstruction with and then without resolution modeling. A direct, measured, normalization was used for $\mathbf{N}_B$, **Bs** was obtained by an analytic single scatter simulation and smoothed delayed-coincidence window data were used for **Br**. Noise in the resulting reconstructions was assessed using the spatial standard deviation of voxel values within a uniform region of the phantom, whilst contrast (*CRC*) was assessed using one of the plastic support rods (4 mm diameter) within the phantom (of zero radioactivity):

$$CRC = (B - C)/B \qquad (8)$$

where B is the mean voxel value in the background region, and C the mean value in the region of the support rod.

IV. Results

A. Simulation Phantom

Figs. 2 and 3 show slices from the six reconstructions of the simulated phantom data, focusing on the transverse slice which included the 49 point sources, to facilitate a visual comparison of the reconstructed image quality. It is visually evident that the greatest difference in image quality is attributable to the inclusion or exclusion of image space resolution modeling. In the reconstruction a 2 mm Gaussian was used to model image space resolution – chosen to correspond exactly to the function used in the Monte Carlo simulation (note that the kernel of equation (7) based on measured data was not used). There is slight degradation in image quality when the list-mode data are reduced to span 3 and span 9 sampling rates, but the difference is relatively minor compared to that associated with the choice of system model.

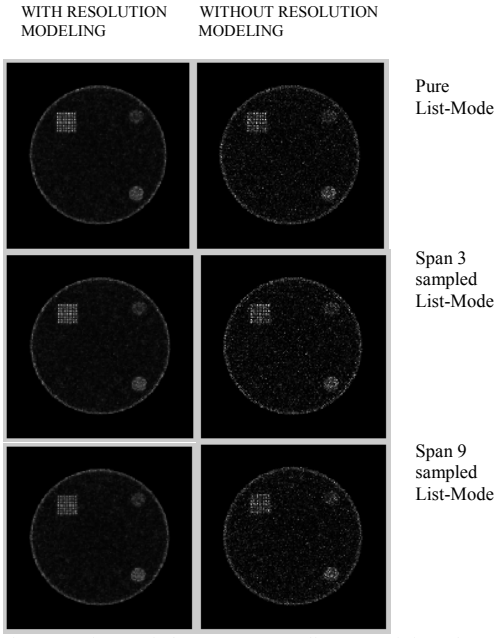

Fig. 2. Visual comparison of the transverse slice containing the 49 point sources for the 6 reconstructions carried out in this study. 2 iterations of 32 subsets were used.

Figs. 4 to 7 indicate the resolution noise trade-off for different stages in the iterative reconstruction for the six reconstructions performed in this study. The graphs confirm that the greatest improvement in image quality arises from the inclusion of an image space resolution model. Pure list-mode and span 3 data behave in a very similar way for the figures of merit used here, with span 9 data beginning to reflect some losses in image quality, particularly for the case of axial (z) resolution, as indicated in Fig 5.

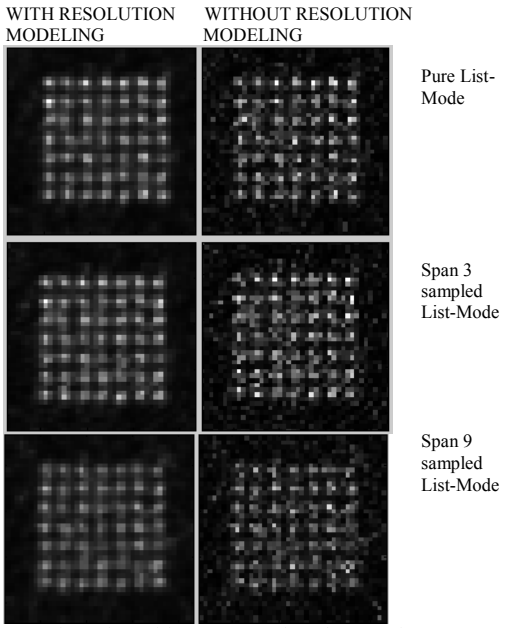

Fig. 3. Same as Fig. 2, but with a zoom to view the 49 point sources.

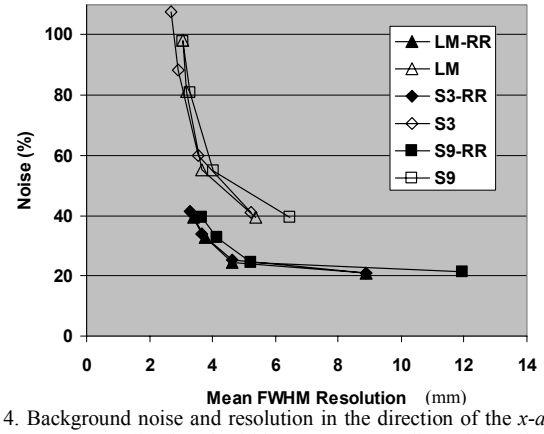

Fig. 4. Background noise and resolution in the direction of the *x-axis* for the line source *vertically* placed within a transverse slice of the phantom. LM indicates pure list-mode data was used, with S3 and S9 indicating that span 3 or span 9 sampling was used. RR indicates that resolution modeling was included. The 4 points on the graph obtained for each of the 6 reconstructions correspond to: first iteration after 16 subsets, end of first iteration (32 subsets completed), second iteration after 16 subsets and the end of the second iteration (2 iterations, each of 32 subsets completed).

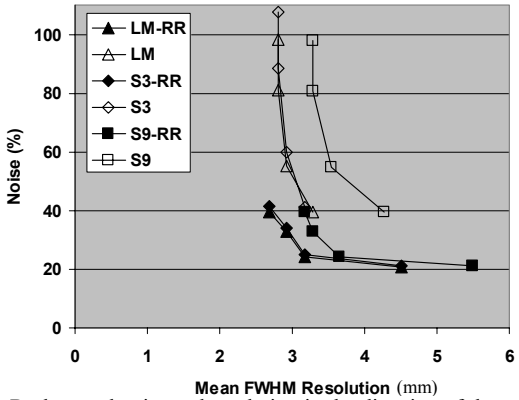

Fig. 5. Background noise and resolution in the direction of the *z-axis* for the line source *vertically* placed within a transverse slice of the phantom.

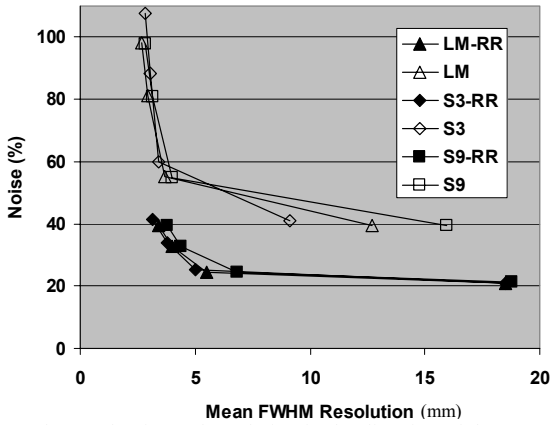

Fig. 6. Background noise and resolution in the direction of the *y-axis* for the line source *horizontally* placed within a coronal slice of the phantom.

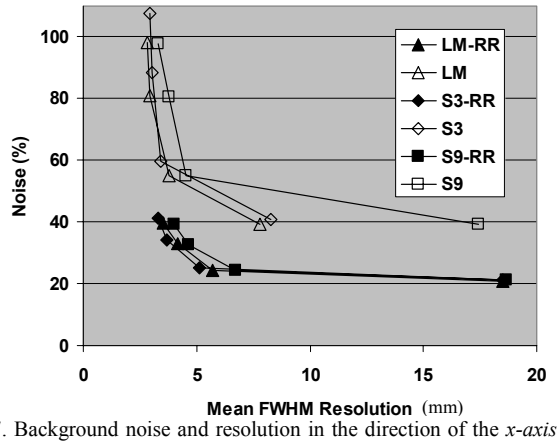

Fig. 7. Background noise and resolution in the direction of the *x-axis* for the line source *horizontally* placed within a coronal slice of the phantom.

B. Measured Data

For the resolution kernel the fit parameters for equation (7) were found to be $\beta=3.11\times10^{-5}$ and $\alpha=10.77$ cm^{-1}. Fig. 8 indicates the impact of inclusion of the matrix **H** when using the shift-invariant kernel of equation (7).

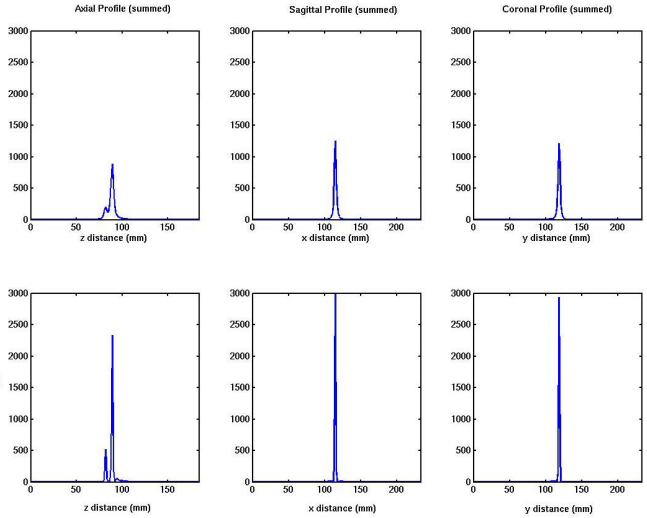

Fig. 8. Impact of resolution modeling on the reconstruction of a central point source – counts are preserved, but more focalized at the location of the point source. Top row: no resolution model. Bottom row: with use of the shift-invariant resolution model.

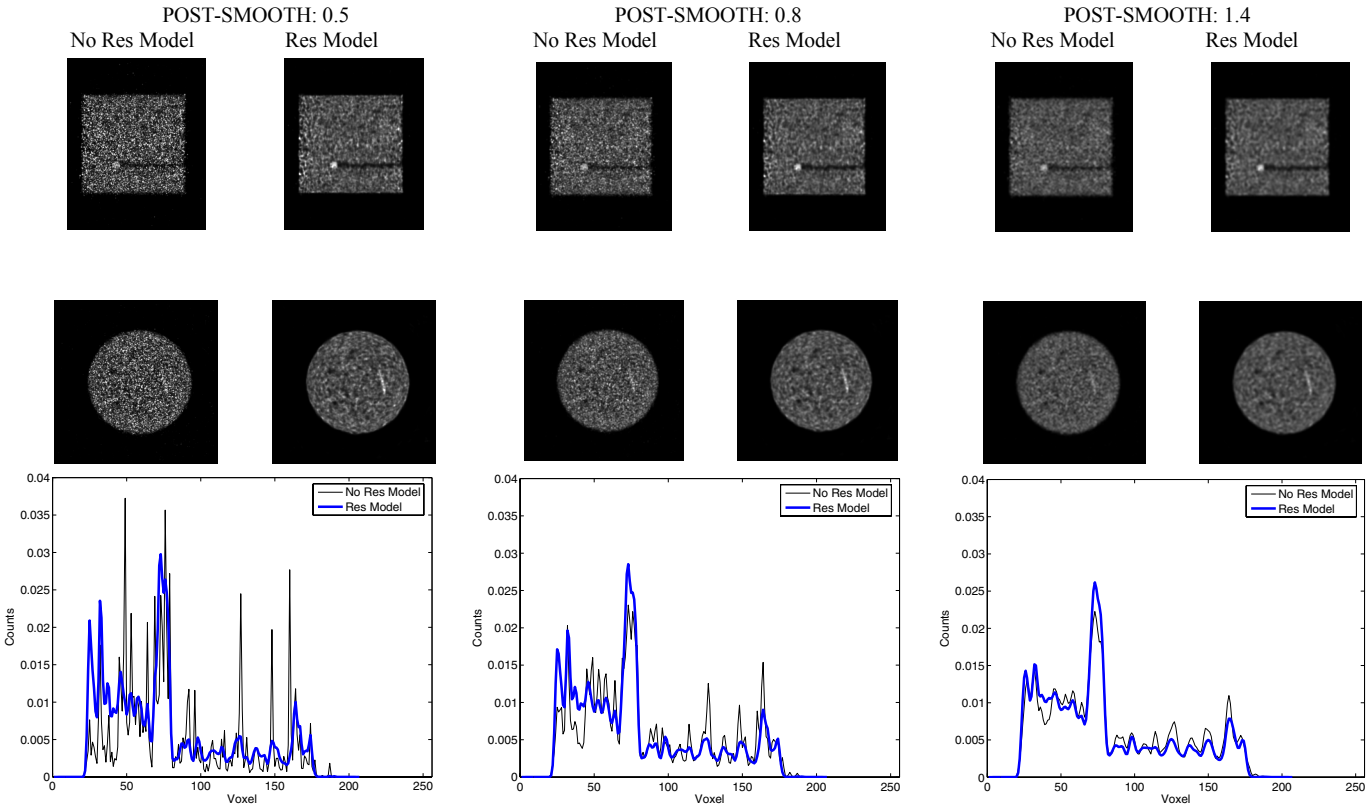

Fig. 9. Slices and profiles from the reconstruction of the Jaszczak phantom for the case of 2 iterations of 96 subsets, and for 3 different levels of post-reconstruction smoothing (using a 3D Gaussian kernel of standard deviation 0.5, 0.8 and 1.4 voxels). A cold supporting rod and a hot sphere are shown in the top row of images (and the profiles), and it is clear that resolution modeling allows good contrast with low noise simultaneously.

Fig. 9 shows example slices and profiles for different levels of post smoothing of the reconstruction images for the Jaszczak phantom. Fig. 10 compares the contrast-noise behavior for different levels of post smoothing, with and without resolution modeling. It is clear again that resolution modeling is central to enhancing image quality for these reconstructed images.

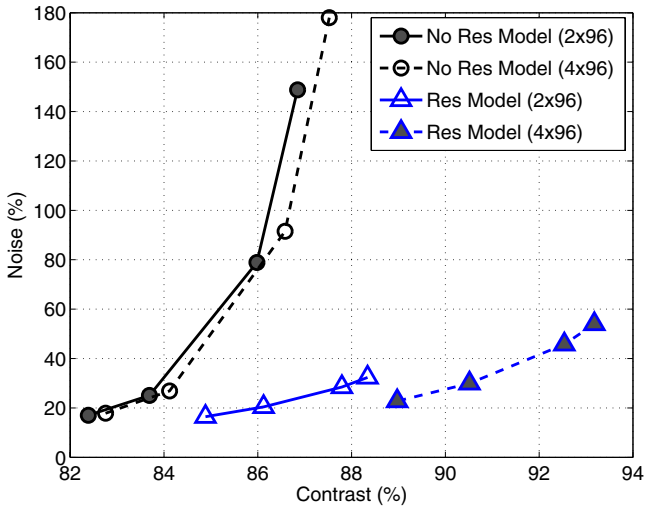

Fig. 10. Noise-contrast behavior for 2 and 4 iterations of 96 subsets, when resolution modeling is included and excluded. The 4 points obtained on the graph for each method correspond to 4 levels of post-reconstruction smoothing.

V. Conclusion

A method for incorporating sinogram data corrections into list-mode iterative reconstruction is presented, which avoids sampling mismatches by spatially aligning each list-mode event to the nearest sinogram bin (the temporal sampling and possible storage advantages of the list-mode data are retained). For the cases considered the difference in image quality between pure list-mode data and span 3 sinograms is minimal, and is far outweighed by the importance of resolution modeling.

References

[1] L. Parra and H.H. Barrett "List-mode likelihood: EM algorithm and image quality estimation demonstrated on 2-D PET" *IEEE Trans. Med. Im.,* vol. 17, pp.228-235, 1998.

[2] A. J. Reader, K. Erlandsson, M. A. Flower and R. J. Ott "Fast accurate iterative reconstruction for low-statistics positron volume imaging" *Phys. Med. Biol*., vol. 43, pp.835-846, 1998.

[3] R. Levkovitz, D. Falikman, M. Zibulevsky, A. Ben-Tal, A. Nemirovski "The Design and Implementation of COSEM, an Iterative Algorithm for Fully 3-D Listmode Data" *IEEE Trans. Med. Im*, vol. 20, pp. 633-642, 2001.

[4] A. Rahmim, M. Lenox, A. J. Reader, C. Michel, Z. Burbar, T. J. Ruth, V Sossi "Statistical list-mode image reconstruction for the high resolution research tomograph" *Phys. Med. Biol*., vol. 49, pp. 4239-4258, 2004.

[5] K. Wienhard, M. Schmand, M.E. Casey, K. Baker, J. Bao, L. Eriksson, W.F. Jones, C. Knoess, M. Lenox, M. Lercher, P. Luk, C. Michel, J.H. Reed, N. Richerzhagen, J. Treffert, S. Vollmar, J.W. Young, W.D. Heiss, R. Nutt "The ECAT HRRT: Performance and First Clinical Application of the New High Resolution Research Tomograph" *IEEE Trans. Nucl. Sci.*, vol. 49, pp. 104-110, 2002.